# The Shape of the Potential Energy Surface and the Thermal Rate Coefficients of the N + $N_2$ Reaction†

**E. Garcia and A. Saracibar**

*Departamento de Quimica Fisica, Universidad del Pais Vasco, Vitoria, Spain*

**A. Laganà* and D. Skouteris**

*Dipartimento di Chimica, Università di Perugia, Perugia, Italy*

*Received: March 24, 2007; In Final Form: May 22, 2007*

Full-dimensional quantum time-dependent calculations of the detailed probabilities of the N + $N_2$ reaction have been performed on different potential energy surfaces, initial quantum states, and total angular momentum quantum numbers. The calculations allowed a rationalization of the effect of both moving the saddle to reaction out of collinearity and lowering its height. On some of these surfaces, more extended studies of the reactive dynamics of the system were performed. On one of them also, thermal rate coefficients were computed using $J = 0$ quantum probabilities and the *J*-shift model after testing the applicability of such a model against centrifugal sudden results. A comparison of the calculated thermal rate coefficients with theoretical and experimental data available from the literature is also made, and possible effects of inserting an intermediate well at the top of the saddle are argued.

## Introduction

The accurate evaluation of state-to-state cross sections and rate coefficients of atom−diatom collisions is a highly demanding computational task. It requires, in fact, full-dimensional quantum calculations of the fixed total angular momentum quantum number *J* detailed **S** matrix elements for several initial states of the reactants. Properly weighed square moduli of the detailed **S** matrix elements are then summed up to convergence with *J*. Such a tremendous computational effort is justified, however, only once the potential energy surface (PES) to be used for the calculations has already proven to be sufficiently accurate. Unfortunately, this is not the case of the popular LEPS PES available from the literature for the nitrogen atom−nitrogen molecule system.[1] Despite that, massive quasiclassical (QCT) and quantum infinite order sudden (RIOS) computational campaigns of the cross sections and thermal rate coefficients have been carried out in quite recent times[2] on the LEPS PES because of their relevance to the modeling of nitrogen plasmas[3] and processes occurring around reentering spacecrafts.[4] More recently, further QCT calculations were performed on the same PES to estimate vibrational relaxation and dissociation rates for the whole ladder of reactant vibrational states.[5−7] Thermal rate coefficients of the N + $N_2$ reaction were also calculated using semiclassical initial value representation and model quantum transition-state methods.[8]

An indication of the inadequacy of the LEPS PES to describe the main features of the interaction of the N + $N_2$ system at the saddle to reaction was first provided by Petrongolo in his ab initio calculations of refs 9 and 10. In particular, his study pointed out that the geometry of the N + $N_2$ system is bent (and not collinear as in the LEPS PES), with a ∠NNN of about 120°. Building on these findings, we assembled four new PESs (L0, L1, L2, and L3; see ref 11) of the so-called generalized rotating bond order (LAGROBO) type.[12,13] On these new PESs, QCT and quantum RIOS calculations[11,14] were performed to analyze the dependence of the reactivity on the geometry of the system at the saddle to reaction.

More recent and extended high-level ab initio calculations (WSHDSP)[15−17] provided more detailed and accurate estimates of the geometry and energy of the system in the strong interaction region. In particular, they singled out the existence of a minimum sandwiched by two barriers (higher than that of the LEPS) along the minimum energy path (MEP) in the strong interaction region. However, thermal rate coefficients computed on the WSHDSP PES did not compare with the experiment as favorably as those computed on the LEPS. To find both the rationalization of the reactive behavior of the N + $N_2$ system and the creation of a suitable set of data for use in spacecraft reentering simulations on a more robust theoretical ground, we carried out extended three-dimensional (3D) quantum calculations on the above-mentioned LEPS and LAGROBO surfaces. Unfortunately, the difficulty of reconstructing the WSHDSP PES from the information given in ref 15 and of obtaining a copy of the related routine from the authors did not allow us to carry out the same calculations on that surface

The paper is organized as follows. In section 2, relevant theoretical and computational details are briefly reviewed; in section 3, the calculated 3D exact quantum reactive probabilities are analyzed, and in section 4, the thermal reactive rate coefficients (obtained from a *J*-shift quantum model treatment) are discussed.

## Theoretical and Computational Details

The method adopted to compute the quantum reactive probabilities of N + $N_2$ stems out of the pioneering work of R. Wyatt[18−20] and is largely based on the time-dependent formalism of G. G. Balint-Kurti and S. K. Gray described in refs 21 and 22. Accordingly, the coordinates used are *R* (the atom−diatom

† Part of the special issue "Robert E. Wyatt Festschrift".

10.1021/jp072345a CCC: $37.00 
Published on Web 07/21/2007

distance), $r$ (the diatomic internuclear distance), and $\Theta$ (the angle formed by $R$ and $r$) for the reactants and the corresponding primed ones for the products. The application of the nuclear Hamiltonian $\hat{H}_N$ to the $\Lambda$ component $\Psi^{J\Lambda}(R, r, \Theta, t)$ of the time-dependent partial wave (shortly $\Psi^{J\Lambda}$) leads to the following expression

$$\hat{H}_N\Psi^{J\Lambda} = [\hat{T}_{R,r,\Theta,J,\Lambda} + V(R, r, \Theta)]\,\Psi^{J\Lambda} + C^J_{\Lambda,\Lambda\pm1}\,\Psi^{J\Lambda\pm1}$$

where (in atomic units)

$$\hat{T}_{R,r,\Theta,J,\Lambda} = \hat{T}_R + \hat{T}_r + \hat{T}_\Theta + \frac{J(J+1) - 2\Lambda^2}{2\mu_R R^2}$$

$$\hat{T}_R = -\frac{\partial^2}{2\mu_R \partial R^2}$$

$$\hat{T}_r = -\frac{\partial^2}{2\mu_r \partial r^2}$$

$$\hat{T}_\Theta = -\left(\frac{1}{2\mu_R R^2} + \frac{1}{2\mu_r r^2}\right)\left(\frac{1}{\sin\Theta}\frac{\partial}{\partial\Theta}\sin\Theta\frac{\partial}{\partial\Theta} - \frac{\Lambda^2}{\sin^2\Theta}\right)$$

$$C^J_{\Lambda,\Lambda\pm1} = \frac{[J(J+1) - \Lambda(\Lambda\pm1)]^{1/2}\,[j(j+1) - \Lambda(\Lambda\pm1)]^{1/2}}{R^2}$$

with $\mu_R$ and $\mu_r$ being the reduced masses of the triatom and the diatom, respectively, in the reactant arrangement.

To start the calculations, a coordinate grid large enough to include both reactant and product asymptotes is constructed. On such a grid, the potential and the complex wavepacket $\Psi^{J\Lambda}$ for a given value of the total angular momentum quantum number $J$ and its body-fixed frame projection $\Lambda$ are calculated. At the beginning ($t = 0$), the system wavepacket $\Psi^{J\Lambda}$ is assembled in the reactant asymptotic region (that is, $R$ is given a value $R_0$ large enough to consider the atom−diatom interaction negligible) in its initial state. This means that at $R_0$, the wavepacket can be formulated as a product of a normalized Gaussian function $Ne^{-\alpha(R-R_0)^2}$, a phase factor $e^{-ik(R-R_0)}$ (with $k$ being the wave vector determining the relative kinetic energy of the collision partners) providing the initial wavepacket with the initial kick toward the strong interaction region, the appropriate Riccati−Hankel functions $h^1_l(k(R - R_0))$, the vibrational wave function $\varphi^{N_2}_{vj}(r)$ of the reactant diatom, and the normalized associated Legendre polynomial $P^\Lambda_j(\Theta)$. Then, the wavepacket is mapped into the product Jacobi coordinate ($R'$, $r'$, and $\Theta'$) space, and diagonal and off-diagonal elements of the remaining part of the Hamiltonian are also calculated on the related grid. The radial kinetic energy terms are evaluated through a fast Fourier transform technique, while the angular terms are calculated through an expansion in a complete Legendre basis set. The wavepacket is then propagated in time after substituting the ordinary Hamiltonian with an analytical function suited to simplify the Chebyshev algorithm. At each stage of the propagation, the overlap of the wavepacket with each of the open asymptotic product channels is calculated and stored in order to evaluate the **S** matrix elements at the end of the time propagation. Near the edge of the grid, an ad hoc complex absorbing potential is added to prevent aliasing effects.

The PESs used for the calculations are, as already mentioned, of the LEPS and the LAGROBO type. The popular LEPS potential ($V^{LEPS}$)[23] for three ($i$, $j$, and $k$) atoms can be expressed using the following many-body formulation

$$V^{LEPS}(r_{ij}, r_{jk}, r_{ik}) = V^{(2-LEPS)} + V^{(3-LEPS)} \quad (1)$$

since the one-body terms are set equal to zero (because only ground electronic states are considered for the N atoms). The two-body term reads

$$V^{(2-LEPS)} = \sum_l {}^1E_l(r_l) \quad (2)$$

with $l$ being the sequential label for the $ij$, $jk$, and $ik$ diatomic pairs and ${}^1E_l(r_l)$ being the Morse diatomic model potential. The three-body (albeit assembled out of two-body contributions) term reads

$$V^{(3-LEPS)} = -\sum_l J_l - \sqrt{\frac{1}{2}\sum_l\sum_{m>l}(J_l - J_m)^2} \quad (3)$$

in which

$$2J_l = {}^1E_l(r_l) - \frac{1-\Delta_l}{1+\Delta_l}\,{}^3E_l(r_l) \quad (4)$$

and ${}^3E_l(r_l)$ is the anti-Morse diatomic model potential; $\Delta_l$ is the $l$th empirical (Sato) parameter, and $D_l$, $\beta_l$, and $r_{el}$ are the dissociation energy, the force constant, and the equilibrium distance of diatom $l$, respectively.

The LAGROBO potentials are, instead, of the many process type and have the form

$$V^{L3}(r_{\tau,\tau+1}, r_{\tau+1,\tau+2}, r_{\tau+2,\tau}) = \sum_\tau w(\Phi_\tau)V^{ROBO}_\tau(\rho_\tau, \alpha_\tau, \Phi_\tau) \quad (5)$$

where $\tau$ (cyclic of module 3) is the process index that indicates also the exchanged atom (for more details, see ref 11). In eq 5, $w(\Phi_\tau)$ ($\Phi_\tau$ being the angle formed by the two bonds having the atom $\tau$ in common) is a weight function having a maximum for collinear contributions ($\Phi_\tau = 180°$) and progressively dying out when moving away from collinearity. In the same equation, $V^{ROBO}_\tau(\rho_\tau, \alpha_\tau, \Phi_\tau)$ is the model rotating bond order (ROBO) potential.[24] The ROBO model potential is formulated in terms of $\rho_\tau$ and $\alpha_\tau$, which are the polar representations of the BO coordinates (with the generic BO coordinate $n_{\tau,\tau+1}$ of the diatom $\tau$, $\tau + 1$ being defined as $n_{\tau,\tau+1} = \exp[-\beta_{\tau,\tau+1}(r_{\tau,\tau+1} - r_{e\tau,\tau+1})]$, in which $\beta_{\tau,\tau+1}$ is a parameter optimized to describe a BO polynomial formulation of a given order of the diatomic potential being considered).

In the simple LAGROBO formulation adopted for N + $N_2$ in ref 11, the ROBO potential reads

$$V^{ROBO}_\tau(\rho_\tau, \alpha_\tau, \Phi_\tau) = D_\tau(\alpha_\tau, \Phi_\tau)\left[\frac{\rho^2_\tau}{a^2_\tau(\alpha_\tau, \Phi_\tau)} - 2\frac{\rho_\tau}{a_\tau(\alpha_\tau, \Phi_\tau)}\right] \quad (6)$$

so as to coincide with the corresponding Morse potential at the asymptotes. The $D_\tau$ and $a_\tau$ coefficients indicate, respectively, the depth and the location in $\rho_\tau$ of the fixed $\Phi_\tau$ MEP of the reaction channel as $\alpha_\tau$ varies from a 0 (reactant) to 90° (product) asymptote. The values $D_\tau$ and $a_\tau$ at the asymptotes ($\alpha_\tau = 0$ and 90°, respectively) were chosen to reproduce the dissociation energy $D_{NN}$, the equilibrium distance $r_{eNN}$, and the exponential factor $\beta_{NN}$ of the $N_2$ Morse diatomic potential ($D_{NN} = 9.90$

**TABLE 1: Saddle Height[a]**

| $\Phi_N$ | LEPS | L0 | L1 | L3 |
|---|---|---|---|---|
| 180° | 1.55 | 1.55 | 3.49 | 3.49 |
| 150° | 1.61 | 1.61 | 1.93 | 1.79 |
| 125° | 1.83 | 1.83 | 1.56 | 1.40 |
| 120° | 1.92 | 1.91 | 1.55 | 1.42 |
| 90° | 3.06 | 3.06 | 2.45 | 2.65 |
| 60° | 7.69 | 7.69 | 7.69 | 7.69 |

[a] Energy in electronvolts.

**TABLE 2: Internuclear N−N Distance[a] at the Saddle**

| $\Phi_N$ | LEPS | L0 | L1 | L3 |
|---|---|---|---|---|
| 180° | 1.240 | 1.240 | 1.240 | 1.240 |
| 150° | 1.243 | 1.244 | 1.244 | 1.244 |
| 125° | 1.251 | 1.252 | 1.252 | 1.252 |
| 120° | 1.254 | 1.254 | 1.254 | 1.254 |
| 90° | 1.294 | 1.293 | 1.293 | 1.293 |
| 60° | 1.530 | 1.522 | 1.522 | 1.522 |

[a] Distance in angstroms of external N atoms from the central one.

**TABLE 3: Input Data for the RWAVEPR Calculations**

| | |
|---|---|
| scattering coordinate ($R'$) range (in $a_0$) | 0−12 |
| number of grid points in ($R'$) | 240 |
| internal coordinate ($r'$) range (in $a_0$) | 0−12 |
| number of grid points in ($r'$) | 240 |
| grid interval (for both $R'$ and $r'$) (in $a_0$) | 0.05 |
| number of angular grid points | 120 |
| potential energy cutoff (in eV) | 5.0 |
| angular kinetic energy cutoffs (in eV) | 5.0,6.5 |
| initial center of the wavepacket (in $a_0$) | 8.5 |
| width of the wavepacket | 0.3 |
| number of Taylor terms | 80 |
| absorbing boundary parameter ($x$,$y$) (in $a_0$) | 11.0 |
| width of the absorbing potential (in $a_0$) | 2.0 |
| position of the analysis line, $R'_\infty$ | 10 |
| number of iterations for $v \leq 1$ | 2000 |
| number of iterations for $v \geq 2$ | 3000 |

eV, $r_{eNN} = 1.0977$ Å, and $\beta_{NN} = 2.689$ Å$^{-1}$ [25]). Again, in order to keep the formulation of the potential as simple as possible, $D_\tau$ and $a_\tau$ were given a linear dependence on sin $\alpha_\tau$.

As already mentioned, our study is focused on the LEPS and on some LAGROBO PESs proposed in ref 11 (namely, L0, L1, and L3). The characteristics at the saddle to reaction of these potentials are given in Tables 1 and 2. The high flexibility of the LAGROBO functional form allows us to shape the L0 PES so as to have the same geometry and energy at the saddle as that for the LEPS. For the L1 PES, instead, the flexibility of the LAGROBO functional is used to lower $\Phi_N$ from 180 down to 120° while leaving the N(external)−N(internal) bond lengths unaltered. Finally, for L3, the geometry of the system at the saddle is set equal to that of L1, while the associated energy is lowered by 0.15 eV (that is, approximately the difference in zero-point energy between the reactants and the transition state).

### Quantum Detailed Reactive Probabilities

To carry out the actual 3D quantum calculations, use is made of the time-dependent wavepacket RWAVEPR[26,27] program and of the input parameters given in Table 3. Thanks to the recent development of distributed computing platforms and technologies,[28−30] it has been possible to run massive calculations of the reaction probabilities (despite the non-light mass of the atoms involved in the process). State ($vj$)-to-state ($v'j'$) partial 3D quantum reactive probabilities, $P^J_{vj,v'j'}$, are evaluated from the detailed **S** matrix elements using the equation

$$P^J_{vj,v'j'}(E_{tr}) = \frac{1}{(2j+1)} \sum_{\Lambda=-\Lambda_{max}}^{\Lambda_{max}} \sum_{\Lambda'=-\Lambda'_{max}}^{\Lambda'_{max}} |S^J_{vj\Lambda,v'j'\Lambda'}(E_{tr})|^2 \qquad (7)$$

where $E_{tr}$ is the relative collision energy and $\Lambda_{max} = \min(j, J)$. In eq 7, the **S** matrix elements are set equal to twice the value calculated for a single product arrangement channel. From the state-to-state partial state-specific quantum reactive probabilities, $P^J_{vj}$ values are computed by summing over the final vibrotational states. In this summation, probabilities for even $j'$ states contribute twice when the nuclear spin of the N atom is one.[31] Out of the state-to-state probabilities also, excitation functions and product vibrational (PVD) and rotational (PRD) distributions are worked out for several $J$ values and initial vibrational and rotational states of the reactants. In particular, to compare the reactive efficiency of the system on the considered PESs, exact $J = 0$ state-to-state quantum reactive probabilities (excitation functions) are calculated for the ground rotational level of the first six vibrational states of the reactant $N_2$ molecule and $E_{tr}$ ranging from threshold up to 2 eV in steps of 0.001 eV.

A first batch of calculations is performed on the LEPS and on the L0 PESs. Plots of the reactive probability values calculated at $J = j = 0$ and $v$ varying from 0 to 5 are given in Figure 1 as solid and dotted lines, respectively. The 3D quantum probabilities, although differing in absolute value from QCT and RIOS ones, confirm that, as expected, results obtained on LEPS and L0 are almost coincident. When calculations are performed also on L1 (to investigate the effect of moving the barrier to reaction out of collinear geometries while preserving its height), the net result is, at $v = 0$ (see dashed-dotted lines of Figure 1), a clear increase of the threshold energy and an associated strong decrease of the reactive probability about the threshold region (in the temperature range of interest, this means also a substantial decrease of the thermal rate coefficient). When the calculations are extended to L3 (to investigate the effect of lowering the saddle to reaction in an attempt to contrast the decrease of the reactivity due to the adoption of a bent geometry at the saddle), the net result (see dashed lines of Figure 1) is a lowering of the threshold energy back almost entirely to the L0 value and a sharp increase of the reactive probability in the energy region immediately following the threshold. This puts on an exact quantum ground the traditional QCT finding that on collinearly dominant PESs, relative collision energy is exploited better than any other mode to the end of enhancing reactivity. Such an effect is particularly strong, however, only at $v = 0$ and for the just-past-the-threshold energy values. At larger $v$ values, in fact, the picture is partially modified. The higher reactive efficiency of the collinearly dominated PESs (LEPS and L0) becomes weaker, and the interplay between larger amounts of vibration and collision energy becomes so strong to efficiently enhance the reactivity also on PESs having a bent geometry at the saddle to reaction, provided that the height of the barrier has been lowered as in L3. As shown by the dashed-dotted lines of Figure 1, in fact, L1 results (for which the barrier has not been lowered) remain lower than the reactive probabilities calculated on the other surfaces for a larger interval of relative collision energy even at $v = 5$.

A first consideration to make, at this point, is that the LAGROBO PESs, which have a bent transition-state geometry (such as L1 and L3), are able to emulate the reactive efficiency of the collinearly dominant PESs (such as the LEPS and L0) only when the barrier to reaction is properly lowered (in our case, as already mentioned, this amount corresponds to the zero-point difference between the transition state and the asymptote.

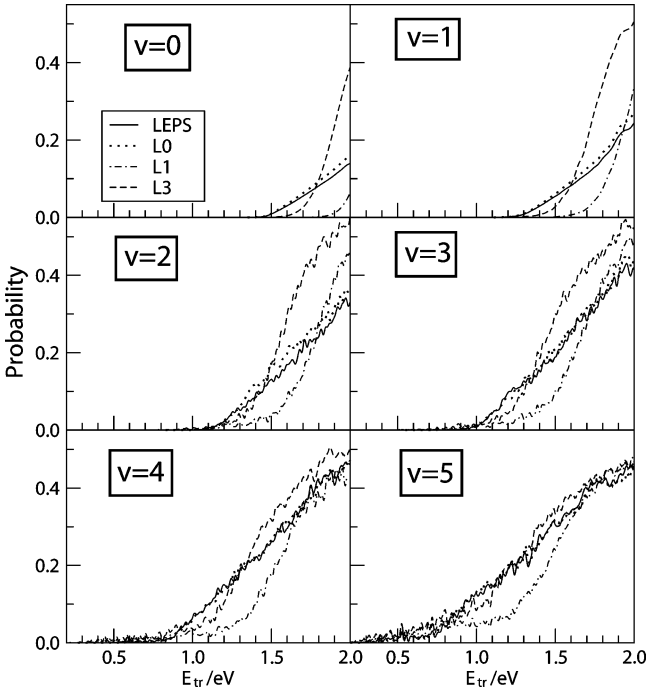


**Figure 1.** State-specific reactive probabilities, $P^J_{ij}(E_{tr})$, calculated on the LEPS (solid line), L1 (dotted line), L1 (dashed-dotted line), and L3 (dashed line) PESs for $v = 0$, 1, 2, 3, 4, and 5 at $j = J = 0$, plotted as a function of the collision energy $E_{tr}$.

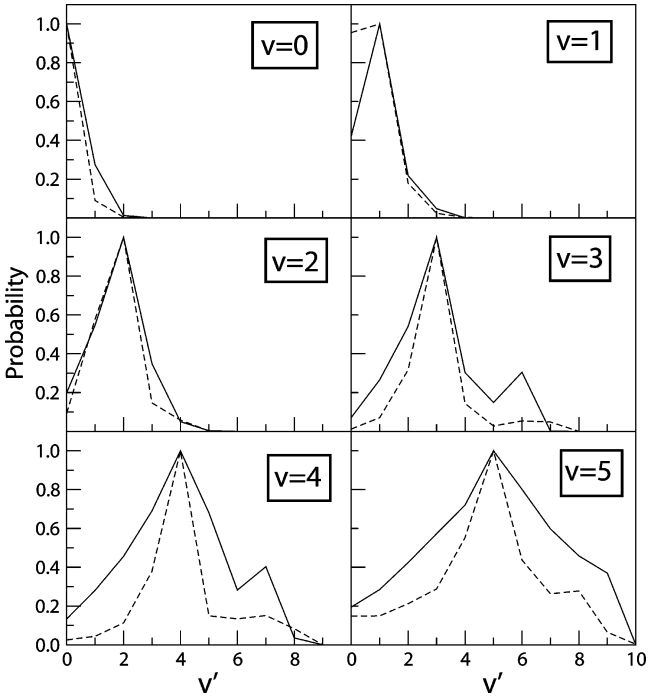


**Figure 2.** Product vibrational distributions calculated on the LEPS (solid line) and L3 (dashed line) PESs for $v = 0$, 1, 2, 3, 4, and 5 at $j = J = 0$ and $E_{tr} = 1.65$ eV, plotted as a function of the product vibrational state $v'$. Distributions are normalized to their maxima.

To consider other properties of the N + $N_2$ reactive system, we shall focus hereafter on the comparison between the LEPS and L3 results. As a first example, we consider here the (normalized to the maximum) PVDs calculated at a collision energy of 1.65 eV. As apparent from Figure 2, the PVD calculated at $v = 0$ shows the substantial vibrational adiabaticity of the related reactive process on both the LEPS and the L3 PESs. A similar feature is also shown by the PVDs calculated at $v = 2$, though with a wider distribution over the product states. Vibrational adiabaticity progressively deteriorates as $v$ increases to 3, 4, and 5, as shown by the progressive extension of the higher $v'$ branch of the distribution. The efficiency in promoting the system to more excited vibrational states is so pronounced for the LEPS PES to generate a second peak at large $v'$ values. On the contrary, not only does L3 show a weaker tendency to produce more vibrationally excited products, but it also shows a marked deexcitation at $v = 1$.

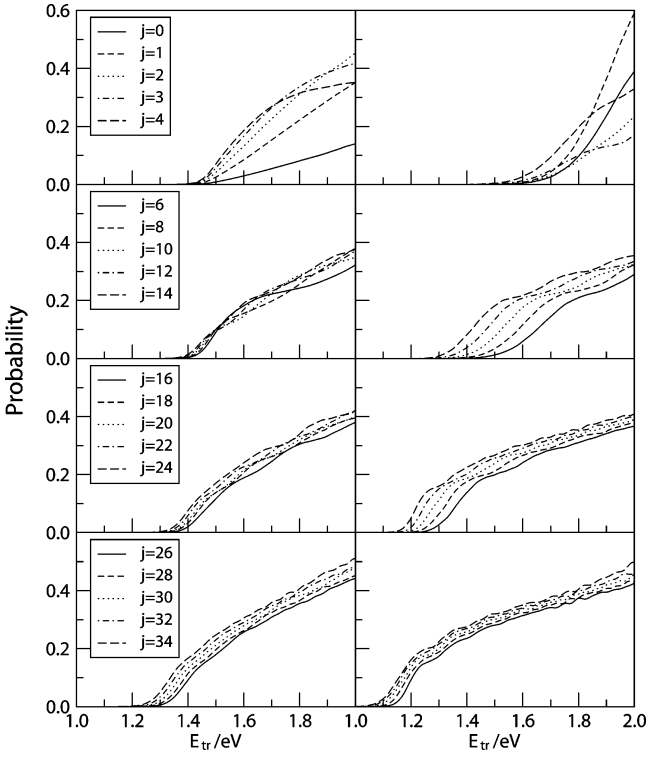


**Figure 3.** State-specific reactive probabilities, $P^J_{ij}(E_{tr})$, calculated on the LEPS (left panels) and L3 (right panels) PESs at $v = J = 0$ and $j = 0-4$ (upper panel), $j = 6-14$ (central upper panel), $j = 16-24$ (central lower panel), and $j = 26-34$ (lower panel), plotted as a function of collision energy $E_{tr}$.

Further interesting information about the dynamical behavior of the N + $N_2$ system on L3 and the LEPS is also obtained by plotting the reactive probabilities at increasing rotational excitation of the reactant molecule. For illustrative purposes, state-specific reactive probabilities calculated on both surfaces (at $v = 0$) are plotted in Figure 3. As is apparent from the figure, while at low $j$ values, the threshold energy is definitely higher for L3 results; it gradually shifts to lower energy as $j$ increases (while the corresponding shift down of the LEPS results is much less appreciable). The two effects become comparable only around $j = 30$. This confirms that the already commented inefficient exploitation of the relative collision energy near the threshold to enhance reactivity on L3 is largely compensated by an efficient exploitation of the other degrees of freedom (contrary to what happens on the LEPS PES). The lowering of the threshold with $j$ is also accompanied by a simultaneous increase of the reactive probability on L3 that is significant mainly at low $j$ values. No such effect is found on the LEPS PES.

As discussed in detail in refs 16 and 17, probabilities calculated on the WSHDSP PES show a definitely rich structure. Such a structure, as already discussed by the authors, is to a large extent associated with the existence of an intermediate

well sandwiched by two equal barriers to reaction. However, no attempt was made by them to investigate how a change in shape of the saddle to reaction would affect the overall reactivity. From the discussion made before on the effect of the location of the barrier on the efficient use of the internal degrees of freedom of the reactants to promote reactivity, we can argue that the shape of the intermediate well must have, at least, an indirect promoting effect on the $N + N_2$ reactivity by displacing the early and late barriers to larger distances. This consideration will turn to be useful in the next section when analyzing the thermal rate coefficients.

### Thermal Rate Coefficients

To calculate thermal rate coefficients and compare them with the experiment[32−34] (which is, after all, the ultimate goal of our investigation), we shall first work out of the state-specific probabilities the integral reactive state-specific cross sections using the expression

$$\sigma_{vj}(E_{tr}) = \frac{\pi}{k_{vj}^2}\sum_{J=0}^{\infty}(2J+1)P_{vj}^{J}(E_{tr}) \tag{8}$$

where $k_{vj}$ is the wavenumber of the system in the $vj$ state. As described in greater detail elsewhere,[22,35,36] by integrating over $E_{tr}$ and averaging (taking into account the different degeneracy for even and odd rotational states) over the $vj$ initial states, one can calculate the corresponding thermal rate coefficient $k(T)$.

The use of eq 8 implies the integration of the Schrödinger equation at all of the populated $vj$ initial states, all of the total angular momentum quantum numbers $J$ contributing to reaction, and all of the allowed values of the $J$ projection $\Lambda$. This makes the size of the single $vj$ calculations proportional to $J^2$ frustrating, in practice, for all of the attempts to carry out an exact calculation converged with $J$. A reasonable compromise between accuracy and feasibility is often obtained by adopting a centrifugal sudden (CS) approach.[22] The CS treatment makes the calculations' block diagonal in $\Lambda$ (with the size of each block not exceeding that of the $J = 0$ one) and particularly suited for running on distributed computational platforms. Due to the large number of involved partial waves, even for moderately heavy systems (like the $N + N_2$ considered here), the calculations are often further simplified by adopting the popular $J$-shift model.[35,36] In the $J$-shift model, the exact calculations are performed only for $J = 0$ ($P_{vj}^{J=0}(E_{tr})$). Then higher $J$ probabilities ($P_{vj}^{J}(E_{tr})$) are worked out by shifting $P_{vj}^{J=0}(E_{tr})$ in energy as follows

$$P_{vj}^{J}(E_{tr}) = P_{vj}^{J=0}(E_{tr} - \Delta E^{J}) \tag{9}$$

with $\Delta E^J$ being defined as

$$\Delta E^{J} = BJ(J+1) \tag{10}$$

and corresponding to the rotational energy of the rigid collinear triatom geometry associated with the saddle to reaction.

When the saddle of the surface is bent, one can still fit the $\Lambda = 0$ probabilities calculated at different $J$ values using eq 10 as an empirical formula. However, it is more appropriate to make the probability shift depend also on $\Lambda$ as follows

$$P_{vj}^{J}(E_{tr}) = \frac{1}{2\Lambda_{max}+1}\sum_{\Lambda=-\Lambda_{max}}^{\Lambda_{max}} P_{vj}^{J=0}(E_{tr} - \Delta E^{J\Lambda}) \tag{11}$$

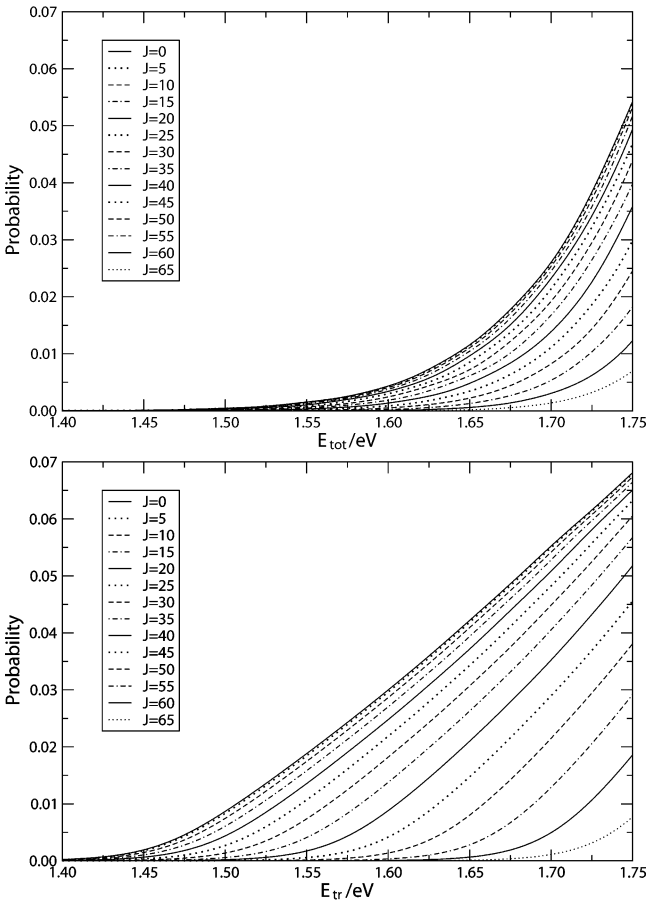


**Figure 4.** CS state-specific reactive probabilities, $P_{vj}^{J\Lambda}(E_{tr})$, calculated on the LEPS (lower panel) and L3 (upper panel) PESs for $v = j = \Lambda = 0$ at various values of $J$ (increasing in going from the left to the right-hand side lines), plotted as a function of collision energy $E_{tr}$.

with $\Delta E^{J\Lambda}$ being defined as

$$\Delta E^{J\Lambda} = \bar{B}J(J+1) + (A - \bar{B})\Lambda^2 \tag{12}$$

which is based on the approximation that the geometry of the system at the bent saddle is a symmetric top one, where $\bar{B} = (B + C)/2$ with $A$, $B$, and $C$ being the three rotational constants of the triatom at the saddle. A less detailed $J$-shift formulation of the rate coefficient based on the classical formulation of the rotational partition function at the saddle[35] is given by

$$k(T) = \sqrt{\frac{\pi(k_B T)^3}{A\,B\,C}}\,k^{J=0}(T) \tag{13}$$

where $k_B$ is the Boltzmann constant and $k^{J=0}(T)$ is the value of the rate coefficient obtained when retaining only the $J = 0$ term in the sum of eq 8.

To check the applicability of the $J$-shift model to the $N + N_2$ reaction, we computed the CS reactive probability at $v = j = \Lambda = 0$ for several $J$ values. The calculated state-specific CS probabilities are plotted in the lower panel of Figure 4 for the LEPS and in the upper panel of the same figure for L3. The figure shows a clear regular spacing in both sets of curves as $J$ increases. Moreover, when the homologous values of the reactive probabilities are plotted as a function of $J(J + 1)$, they lie on a straight line (these lines, though, are slightly shifted for different probability values). For the LEPS probabilities, the slopes of these lines are all close to the value of the rotational constant $B$ (see eq 10) of the collinear NNN geometry at the

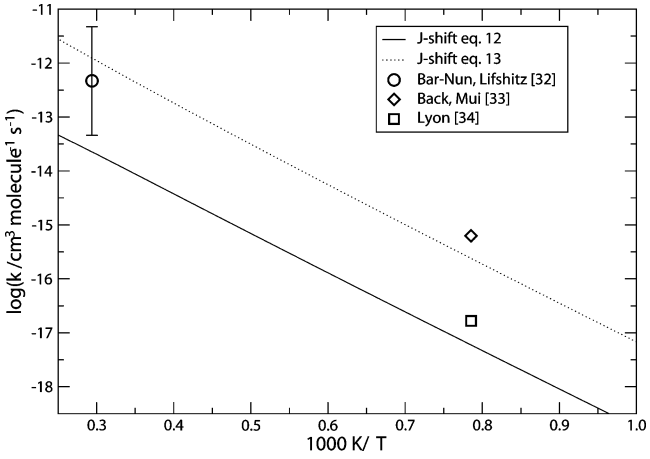


**Figure 5.** Logarithm of the rate coefficient plotted as a function of the inverse temperature using the two *J*-shift models. Experimental data of ref 32 (circle), of ref 33 (diamond), and of ref 34 (square) are also shown. It is worth noting that experiments at $T = 1273$ K only give upper limits for the rate coefficient.

reaction saddle. The calculated average value of $B$ coincides (within an error of 10%) with the theoretical one ($4.9 \times 10^{-5}$ eV) derived from the value of the coordinates of the system geometry at the saddle. A similar treatment was also applied to the L3 results using the probability values plotted in the upper panel of Figure 4. In this case, however, due to the bent geometry of the system at the saddle, eq 12 was used to fit the $v = j = \Lambda = 0$ probabilities. From this, a value of $\bar{B}$ (that is equal to the average of $B$ and $C$) of $2.0 \times 10^{-5}$ eV was obtained. On the contrary, a calculation of the rotational constants of the system at the bent geometry of the L3 transition state gives for $A$, $B$, and $C$ values of $6.7 \times 10^{-4}$, $6.0 \times 10^{-5}$, and $5.5 \times 10^{-5}$ eV, respectively. This leads to a $\bar{B}$ value about 2.5 times larger than the one obtained from a fitting of the calculated probabilities (that, given the assumptions made, is a more than acceptable result).

In order to be able to use the previously described *J*-shift models to evaluate the thermal rate coefficients, the exact $J = 0$ calculations were repeated for the $j$ intervals 0−82 at $v = 0$, 0−74 at $v = 1$, 0−62 at $v = 2$, and 0−50 at $v = 3$. In this way, it was possible to include all of the reactant vibrational states appreciably populated in the temperature range covered by the experiment (1000−4000 K). The usual log $k(T)$ versus $1/T$ plots for the *J*-shift models discussed above together with the experimental results of refs 32−34 are given in Figure 5.

The first feature of these results that deserves to be emphasized here is the fact that the thermal rate coefficient values calculated on L3 using the *J*-shift model of eq 12 fall slightly short of the measured data at both $T = 3400$ and 1273 K, while sufficiently well reproducing their trend with the inverse temperature. This marks a clear difference with the (larger) ones obtained still on L3 when using the more approximate eq 13.

A more quantitative comparison of the calculated thermal rate coefficient values at the temperatures of the experiment is given in Table 4 in which results obtained from other approaches are also shown. An apparent feature of the results given in the table is that the thermal rate coefficient values calculated on L3 using the *J*-shift model of eq 12 are always appreciably smaller than the QCT and RIOS ones (see ref 11 for additional data). The *J*-shift values calculated on L3 are also always smaller than those calculated on the LEPS, as are those calculated on the WSHDSP PES. These two quantum results, however, have a clearly different trend with temperature. Thermal rate coefficient values calculated on L3, in fact, are smaller than those calculated on the WSHDSP PES at $T = 3400$ K, while they are larger at $T = 1273$ K. According to our analysis of the dependence of the reactive probability on the various internal energy modes, this may be due to the fact that at low temperatures, the system has easier access to the (lower) saddle to reaction of L3 than to the (higher) WSHDSP one. On the contrary, at the temperature of 3400 K, when the saddle can be more easily accessed on both surfaces, the fact that the WSHDSP PES has a barrier displaced in the entrance channel (as is typical of collinearly dominant reactions like the LEPS and the L0 PESs) allows it to more efficiently exploit the collision energy and gain larger reactivity. These findings clearly indicate that L3 has to be improved by enforcing the reproduction of the intermediate structure shown by ab initio calculations not only because this will improve its reproduction of the ab initio structural data but also because it will improve the agreement with dynamical information provided by the measured thermal rate coefficients. However, the above-discussed results indicate also that, before carrying out an improved fit of the existing ab initio data, further efforts should be spent to investigate whether the depth and the width of the intermediate well should be deepened and widened, respectively, as a result of specifically targeted higher level ab initio calculations.

**TABLE 4: Logarithm of the Rate Coefficients (in $cm^3$ $molecule^{-1}$ $s^{-1}$)**

| | $T = 3400$ K | $T = 1273$ K |
|---|---|---|
| experiment from ref 32 | $-12.3 \pm 1.0$ | |
| experiment from ref 33 | | $<-15.2$ |
| experiment from ref 34 | | $<-16.9$ |
| QCT on LEPS from ref 5 | −12.2 | −16.2[a] |
| QCT on L3 from ref 11 | −11.8 | − |
| RIOSA on LEPS from ref 11 | −12.3 | − |
| RIOSA on L3 from ref 11 | −12.0 | − |
| quantum (*J*-shift) on LEPS from ref 15 | −12.7 | −15.9 |
| quantum (*J*-shift) on WSHDSP from ref 15 | −13.0 | −18.5 |
| quantum (*J*-shift using eq 12) on L3 | −13.6 | −17.2 |
| quantum (*J*-shift using eq 13) on L3 | −11.9 | −15.6 |

[a] Extrapolated value.

## Conclusions

The quantum study of the N + $N_2$ system discussed in this paper was prompted by the need to understand why thermal rate coefficients computed on the LEPS PES (unable to reproduce the bent geometry of the system at the saddle to reaction suggested by the ab initio potential energy calculations) compare with the experiment sufficiently well while those computed on the WSHDSP one (tailored to suite the above-mentioned ab initio potential energy values) do not. To investigate how reactive probabilities change when modifying the characteristics of the saddle to reaction, we performed 3D quantum calculations on L0 (a LAGROBO PES reproducing the height of the barrier to reaction and the collinear dominance of the LEPS), L1 (a LAGROBO PES having a bent geometry at the saddle to reaction while preserving its height and stretch of the two opposite bonds), and L3 (the same as L1 but with a barrier to reaction lowered by the difference in zero-point energy between reactants and the transition state) previously proposed in the literature. This has offered us a way to rationalize the variation of the calculated reactive probabilities as a function of collisional, vibrational, and rotational energies, despite the impossibility of accessing the WSHDSP PES to produce new results.

However, a comparison of our results with those obtained on the WSHDSP PES and available from the literature pointed out some peculiar dynamical effects associated with PESs having a bent saddle to reaction. In particular, the calculations provided valuable information on the role played by internal (vibration and/or rotation) energy to the efficiency of the reaction and to the adiabaticity of the state-to-state processes. They have also been used to investigate the applicability of the *J*-shift models to calculate thermal rate coefficients of the $N + N_2$ reaction. This gave us the possibility of calculating accurate estimates of thermal rate coefficients on L3 and inferring possible consequences on the reactivity of displacing the barriers farther in the asymptotic region.

**Acknowledgment.** Partial financial support from MEC, MIUR, and ARPA Umbria is acknowledged. Computational resources provided by the SGI of the University of the Basque Country, by the Barcelona Supercomputing Center, and by the EGEE Grid project are also acknowledged. This work has been carried out as part of the activities of the working group QDYN of the COST CMST European Cooperative Project CHEMGRID (Action D37).

## References and Notes

(1) Laganà, A.; Garcia, E.; Ciccarelli, L. *J. Phys. Chem.* **1987**, *91*, 312.
(2) Laganà, A.; Garcia, E. *J. Phys. Chem.* **1994**, *98*, 502.
(3) Armenise, I.; Capitelli, M.; Garcia, E.; Gorse, C.; Laganà, A.; Longo, S. *Chem. Phys. Lett.* **1992**, *200*, 597.
(4) Armenise, I.; Capitelli, M.; Celiberto, R.; Colonna, G.; Gorse, C.; Laganà, A. *Chem. Phys. Lett.* **1994**, *227*, 157.
(5) Esposito, F.; Capitelli, M. *Chem. Phys. Lett.* **1999**, *302*, 49.
(6) Esposito, F.; Armenise, I.; Capitelli, M. *Chem. Phys.* **2006**, *331*, 1.
(7) Esposito, F.; Capitelli, M. *Chem. Phys. Lett.* **2006**, *418*, 581.
(8) Faginas Lago, N.; Laganà, A.; Gargano, R.; Barreto, P. R. P. *J. Chem. Phys.* **2006**, *125*, 114311.
(9) Petrongolo, C. *J. Mol. Struct.* **1988**, *175*, 215.
(10) Petrongolo, C. *Mol. Struct.:THEOCHEM* **1989**, *202*, 135.
(11) Garcia, E.; Laganà, A. *J. Phys. Chem. A* **1997**, *101*, 4734.
(12) Garcia, E.; Laganà, A. *J. Chem. Phys.* **1995**, *103*, 5410.
(13) Laganà, A.; Ochoa de Aspuru, G.; Garcia, E. *J. Chem. Phys.* **1998**, *108*, 3886.
(14) Laganà, A.; Ochoa de Aspuru, G.; Garcia, E. *Temperature Dependence of Quasiclassical and Quantum Rate Coefficients for* $N + N_2$; Centro Stampa, Universita di Perugia: Perugia, Italy, 1996.
(15) Wang, D.; Stallcop, J. R.; Huo, W. M.; Dateo, C. E.; Schwenke, D. W.; Partridge, H. *J. Chem. Phys.* **2003**, *118*, 2186.
(16) Wang, D. Y.; Huo, W. M.; Dateo, C. E.; Schwenke, D. W.; Stallcop, J. R. *Chem. Phys. Lett.* **2003**, *379*, 132.
(17) Wang, D.; Huo, W. M.; Dateo, C. E.; Schwenke, D. W.; Stallcop, J. R. *J. Chem. Phys.* **2004**, *120*, 6041.
(18) McCullough, E. A., Jr.; Wyatt, R. E. *J. Chem. Phys.* **1969**, *51*, 1253.
(19) McCullough, E. A., Jr.; Wyatt, R. E. *J. Chem. Phys.* **1971**, *54*, 3578.
(20) McCullough, E. A., Jr.; Wyatt, R. E. *J. Chem. Phys.* **1971**, *54*, 3592.
(21) Balint-Kurti, G. G.; Gray, S. K. *J. Chem. Phys.* **1998**, *108*, 950.
(22) Balint-Kurti, G. G. *Lect. Notes Chem.* **2000**, *75*, 15.
(23) Hirst, D. M. *Potential Energy Surfaces, Molecular Structures and Reaction Dynamics*; Taylor & Francis: London, 1985; p 114.
(24) Laganà, A. *J. Chem. Phys.* **1991**, *95*, 2216.
(25) Huber, K. P.; Herzberg, G. *Molecular Spectra and Molecular Structure. IV Constants of Diatomic Molecules*; Van Nostrand: New York, 1979.
(26) Skouteris, D.; Laganà, A.; Capecchi, G.; Werner, H.-J. *Int. J. Quantum Chem.* **2004**, *96*, 562.
(27) Skouteris, D.; Pacifici, L.; Laganà, A. *Mol. Phys.* **2004**, *102*, 2237.
(28) Laganà, A.; Pacifici, L.; Skouteris, D. *Lect. Notes Comput. Sci.* **2004**, *3044*, 357.
(29) Enabling Grids for E-Science in Europe (EGEE). http://www.eu-egee.org.
(30) European COST Action D37 "Grid Computing in Chemistry: GRIDCHEM". http://www.cost.esf.org/index.php?id=189&action_number=d37.
(31) Herzberg, G. *Molecular Spectra and Molecular Structure. I Spectra of Diatomic Molecules*; Van Nostrand: New York, 1950.
(32) Bar-Nun, A.; Lifshitz, A. *J. Chem. Phys.* **1967**, *47*, 2878.
(33) Back, R. A.; Mui, J. Y. P. *J. Phys. Chem.* **1962**, *66*, 1362.
(34) Lyon, R. *Can. J. Chem.* **1972**, *50*, 1437.
(35) Bowman, J. M. *J. Phys. Chem.* **1991**, *95*, 4960.
(36) Bowman, J. M. *Lect. Notes Chem.* **2000**, *75*, 101.